Sensitivity of Simulated Fire-Generated Circulations to Fuel Characteristics During Large Wildfires

Matthew Roberts [1], Neil P. Lareau [1], Timothy W. Juliano [2], Kasra Shamsaei [1], Hamed Ebrahimian [1], Branko Kosovic [2]

[1] University of Nevada-Reno, Reno, Nevada, USA

[2] National Center for Atmospheric Research, Boulder, Colorado, USA

Corresponding author: Matthew Roberts (matthew.roberts@nevada.unr.edu)

Key Points:

- Coupled fire-atmosphere models struggle to simulate critical fire-generated winds and plume rise during large wildland fires
- Deficient fire-generated winds are linked to inadequate fuel loads and burnout timescale in the model
- Adjustment of the fuel characteristics results in more realistic simulated plumes and fire-generated winds

Abstract

Coupled fire-atmosphere models often struggle to simulate important fire processes like fire generated flows, deep flaming fronts, extreme updrafts, and stratospheric smoke injection during large wildfires. This study uses the coupled fire-atmosphere model, WRF-Fire to examine the sensitivities of some of these phenomena to the modeled surface fuel load. Specifically, the 2020 Bear Fire and 2021 Caldor Fire in California's Sierra Nevada are simulated using three fuel loading scenarios (1x, 4x, and 8x LANDFIRE derived surface fuel), while controlling the fire rate of spread, to isolate the fuel loading needed to produce fire-generated flows and plume rise comparable to NEXRAD radar observations of these events. Increasing fuel loads and corresponding fire residence time in WRF-Fire leads to deep plumes in excess of 10 km, strong vertical velocities of 40-45 m s^{-1}, and combustion fronts several kilometers in width (in the along wind direction). These results indicate that LANDFIRE-based surface fuel loads in WRF-Fire likely under-represent fuel loading, having significant implications for simulating landscape-scale wildfire processes, associated impacts on spread, and fire-atmosphere feedbacks.

Plain Language Summary

Coupled fire-atmosphere models poorly depict large-scale fire processes, such as fire generated winds and deep smoke plumes. In this study, the 2020 Bear Fire and 2021 Caldor Fire in California are simulated under various fuel scenarios. The simulations show that fuel characteristics used in the fire-atmosphere model under-represent observed conditions and thus produce inadequate fire-generated winds and plume characteristics. When the modeled fuels are augmented to match observed fuel load and burnout time, simulated fire-atmosphere feedbacks better resemble fire generated winds and deep convective plumes seen in radar observations. The results of these simulations will help inform future improvements to coupled fire-atmosphere models to better simulate large wildland fires.

1 Introduction

Fire size and intensity has been increasing in the western United States in recent decades (Westerling et al., 2006, 2016; Williams, 2013; Holden et al., 2018; Parks and Abatzaglou 2020). These larger, more intense fires are often characterized by 1000s of acres of simultaneous combustion (i.e., mass fire, Finney and McAllister, 2011), deep convective columns, pyrocumulonimbus (pyroCu/Cb) capable of injecting smoke into the stratosphere (Fromm et al., 2006, 2010; Rodriguez et al., 2020; Peterson et al., 2021), and extreme fire-generated winds including fire-generated tornadic vortices (FGTVs) (Fromm et al., 2006, 2010; Cunningham and Reeder, 2009; Lareau et al., 2018, 2022a). Given the complex threats posed by landscape fires on the social, ecological, and built environments and the expected increase in fire frequency and intensity in a warming climate (Abatzoglou and Williams, 2016; Dowdy et al., 2019), accurate simulation of fires and their impacts are necessary for improved societal resilience, pre-fire planning, and active-fire situational awareness.

Uncertainties in combustion processes, fire spread, fuel representation, and atmospheric feedbacks make simulations of large real-world fires challenging (Peace et al., 2020; Shamsaei et al., 2023a). For example, current fire spread models used in fire-fighting operations such as FARSITE (Finney, 1998) and ELMFire (Lautenberger, 2013, 2017) rely on the semi-empirical Rothermel (1972) rate of spread model but are not coupled to the atmosphere. Thus, these models cannot simulate turbulent flow fields or the feedbacks between fire and atmospheric

processes, such as fire-induced updrafts and associated inflow winds that alter the rate and direction of fire spread. This is problematic in that these fire-induced winds can become the dominant driver of large wildland fires (Coen et al., 2018). Rather, to simulate these feedbacks, coupled fire-atmosphere modes are required, wherein an atmospheric model resolves the wind field that drives fire spread. In turn, the fire's heat and moisture fluxes are released back into the atmosphere, thereby perturbing the wind field, which are then passed back to the fire spread code to represent coupling between the fire and atmosphere (Clark et al., 2004).

WRF-Fire, and the similar WRF-SFIRE, are examples of coupled fire-atmosphere simulation platforms that link the Weather Research and Forecasting (WRF) atmospheric model (Skamarock and Klemp, 2008; Skamarock et al., 2019) with the Rothermel rate of spread model (Rothermel, 1972) to simulate fire spread along with atmospheric responses and feedbacks on the fire (Clark et al., 2004; Mandel et al., 2011; Coen et al., 2013). While these coupled models show promise in simulating perimeter changes in landscape scale fires (Kochanski et al., 2013; Jimenez et al., 2018; DeCastro et al., 2022; Shamsaei et al. 2023a,b; Juliano et al., 2023), thorough validation of the atmospheric response and feedbacks to the fire are lacking outside of small-scale grass fire experiments (e.g., FIREFLUX, FIREFLUX II). For example, most studies validate perimeter changes without providing validation of plume responses or flow modifications, and thus it is possible that these models sometimes produce the right answer (e.g., a correct perimeter) for the wrong reason. This can be problematic in simulations of landscape-scale fires, where atmospheric responses and feedbacks become more important in dictating fire spread and its impacts.

To investigate these model deficiencies, we conduct a sequence of sensitivity tests designed to isolate the role of fuel loading and consumption on simulated fire-generated circulations, including the plume rise and inflow winds. We first motivate this work with an example of the model deficiencies (Section 2), before moving on to our methods, results, and implications (Sections 3-5).

2 Problem Statement

Shamsaei et al. (2023a, b) showed in two recent simulations of California's deadliest fire, the Camp Fire in 2018, that burn area was relatively well depicted by WRF-Fire, however fire and atmospheric feedbacks were deficient in terms of heat release, fire-generated flows, and plume depth. With this in mind, a preliminary simulation of another landscape-scale fire (2020 Bear Fire in California's northern Sierra Nevada; Fig. 1) was conducted using a similar WRF-Fire configuration to that of Shamsaei et al. (2023a, b) based on the operational Colorado Fire Prediction System (CO-FPS; Jimenez et al., 2018). The details of this simulation, including the namelist are contained in supplements S1 and S2. In this preliminary simulation, although WRF-Fire depicts a similar fire perimeter (Fig. 1c) to the observed perimeter (Fig. 1a), comparison with radar observed winds reveals that the simulation lacks both the pronounced region of fire-generated flow reversal and inflow wind opposing the background flow to the west of the head fire (note red shading in Fig. 1a, b) and the deep plume structure that lofts smoke and ash into the mid-troposphere (Fig. 1a-d). Thus, while this operational WRF-Fire configuration produces adequate fire spread, it does not produce the fire-generated winds and plume dynamics that are critical drivers of the fire behavior. The preliminary simulations are further deficient in that they inadequately represent the breadth of the combustion, measured in terms of the satellite observed infrared footprint of the fire (Fig. 2). For example, the broad region of high heat release rates in

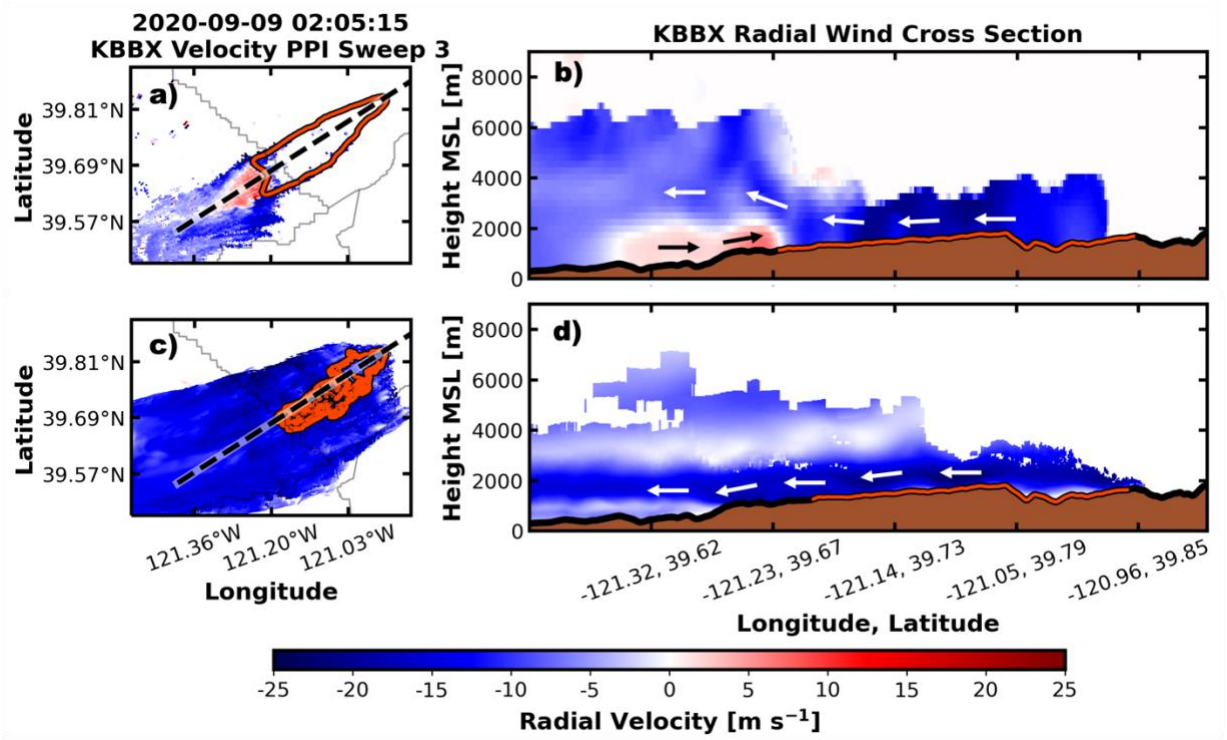

Figure 1. Comparison of observed and simulated fire properties. (a) Beale Air Force Base (KBBX) NEXRAD radial velocity PPI (shaded) and radar-estimated fire perimeter (red contour), (b) radial wind and radar-estimated fire perimeter cross section (red line) along black dashed line in (a), (c) WRF-Fire simulated in-plume radial velocity PPI and fire perimeter, and (d) simulated in-plume radial wind and fire perimeter cross section (red line) along black dashed line in (c) during a period of pronounced fire atmosphere coupling on the Bear Fire around 0200 UTC September 9, 2020. In-plane directional flow vectors annotated in b and d.

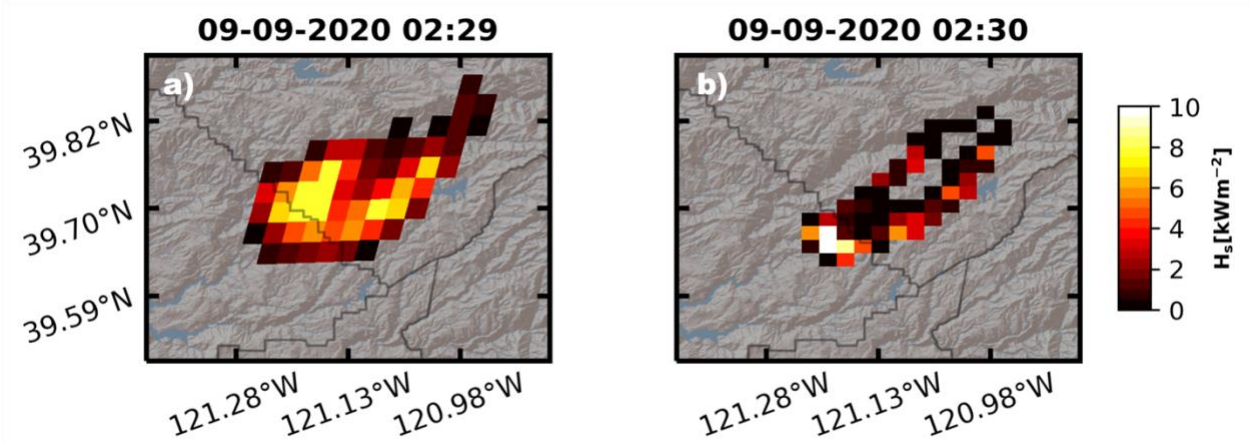

Figure 2. Comparison of (a) GOES-17 Fire-Radiative Power (FRP) converted to sensible heat flux (FRPx10; from Val Martin et al., 2012) with (b) preliminary WRF-Fire sensible heat flux down-sampled to a 2x2 km grid in the Bear Fire.

observations (Fig. 2a) is much larger than that of the preliminary WRF-Fire simulation, even when we resample the WRF output to match the satellite's spatial resolutions (Fig. 2b). While previous studies have noted deficiencies with fuel representations in fire models and their impact on fire perimeter changes (DeCastro et al., 2022; Stephens et al., 2022), the goal of this work is to isolate how fuel characteristics affect fire-generated winds and plume development using observations of these processes as a validation metric.

We hypothesize that exisitng coupled fire-atmosphere models are deficient in producing the observed fire-atmosphere coupling during landscape-scale fires because they have (1) insufficient fuel loads and consumption and (2) inadequate representations of how fires move through the landscape due to inherent limitations of the fire spread model (e.g., lack of mass fire and spotting).

To test these hypotheses, we use WRF-Fire to simulate two landscape-scale wildfires (details below) during periods of strong fire-atmosphere coupling and conduct a series of fuel load sensitivity tests while prescribing the fire's rate of spread. This is accomplished by turning off the model's fire spread code and using a "time-of-arrival" grid (similar to the process described in Farguell et al., 2021) based on radar observations (methodology described in Lareau et al., 2022b). We also modify the fire residence time (i.e., the time required for the fuel to burn down to ~37% of its initial load) to generate broader combusting regions more consistent with the observations. These permutations allow us to determine the threshold fuel loading for WRF-Fire to generate reasonable fire-atmosphere coupling comparable to observations.

3 Data and Methods

3.1 The Fires

The Bear and Caldor Fires in California's Sierra Nevada (see Table 1, Fig. 3) provide ideal test cases to examine WRF-Fire's ability to simulate fire-atmosphere coupling during high-intensity landscape scale fires. Both fires developed deep convective plumes and strong fire-induced winds in similar terrain and fuels, but under strong (i.e., 30 m/s) and light (i.e., 10 m/s) wind scenarios, respectively. Details of the fires are as follows:

The Bear Fire was ignited by lightning on 17 August 2020 in Plumas National Forest in the northern Sierra Nevada. On 8 September the fire was affected by a strong downslope wind event with wind gusts up to 30 m s^{-1} which drove extreme rates of spread, deep pyroCb-topped plumes, and FGTVs (Lareau et al., 2022a, b). The fire ultimately burned approximately 318,935 acres (129,068 ha), destroyed 2,455 buildings, and resulted in 16 fatalities.

The Caldor Fire ignited on 14 August 2021 in Eldorado National Forest in the central Sierra Nevada. On 17 August the fire experienced rapid fire spread and deep pyroCb plumes while advancing eastward across the Sierra Nevada west slope. The fire ultimately burned approximately 221,835 acres (89,773 ha) and destroyed 1,003 buildings (USDA Forest Service, 2021 and CalFire Incident Archive, 2021).

Both fires produced pronounced flow reversals downwind of the head fire (e.g., Fig. 1a,b) and plume echo tops episodically exceeding 10km above mean sea level (MSL) in NEXRAD radar imagery. These strong fire-generated circulations make these cases well suited for model sensitivity tests.

Table 1. Two fire cases identified for sensitivity analysis.

Fire Name	Date of Ignition	Analysis Date(s)	Location	Acres (ha) Burned on Analysis Date(s)	Total Acreage (ha)	Dominant SB40 Fuel Type
Bear Fire	17 August 2020	1900 UTC 8 Sep – 0400 UTC 9 Sep 2020	Plumas National Forest	193,759 (78,411)	318,935 (129,068)	TU5 (69%)
Caldor Fire	14 August 2021	1500 UTC 17 Aug – 0000 UTC 18 Aug 2021	Eldorado National Forest	20,939 (8,474)	221,835 (89,773)	TU5 (73%)

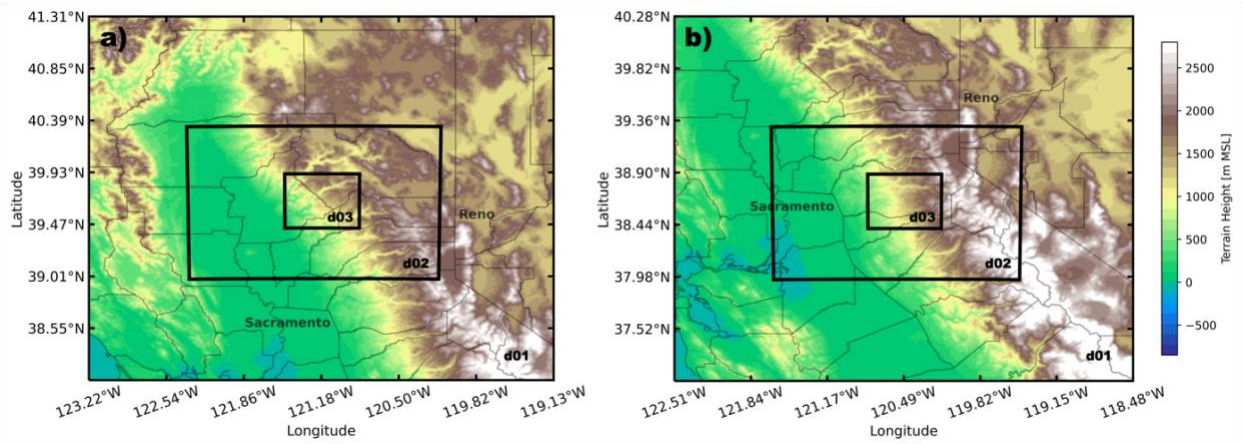

Figure 3. Outer (d01), middle (d02), and inner (d03) domain configuration for the (a) Bear Fire and (b) Caldor Fire with WRF terrain (shaded).

3.2 WRF-Fire

Our simulations are conducted with WRF-Fire (Mandel et al., 2011; Coen et al., 2013). The configuration closely follows that of Jimenez et al. (2018) and Shamsaei et al. (2023a, b). The atmospheric model uses one-way nesting across three domains containing 41 vertical levels up to 50 hPa. The outermost domain has a horizontal grid spacing of 1 km with inner nests of 333 m and 111 m on the atmospheric mesh, with the innermost domain resolving the fire on a further refined mesh with spacing of ~28 m, centered over the fire areas (Fig. 3). The terrain in the inner fire domain is derived from the 30-meter resolution NASA SRTM topographic dataset (van Zyl, 2001; Farr and Kobrick, 2000). The simulations use the 2011 National Land Coverage Database (NLCD2011) (Homer et al., 2015) with Noah land-surface (Chen and Dudhia, 2001) and Revised Monin-Obukhov surface layer (Jimenez et al., 2012) parameterization schemes. The Dudhia (1989) shortwave radiation, Rapid Radiative Transfer Model (RRTMG) longwave radiation (Iacono et al., 2008), and Hong and Lim (2006) WRF single-moment 6-class (WSM6) microphysics schemes are also used. The Mellor-Yamada-Nakanishi-Niino (MYNN; Nakanishi and Niino, 2006) PBL scheme is used on the two outer domains, with the innermost domain resolving turbulence using the subgrid-scale model of Lilly (1966a, b) and Deardorff (1980). Initial and boundary conditions are set using High Resolution Rapid Refresh (HRRR) analysis data (3 km spatial resolution) that update every hour through completion of the simulation.

3.3 Fire Spread and Perimeters

In its operational configuration, WRF-Fire uses the Rothermel ROS model (Rothermel, 1972) to propagate fire across a landscape. The Rothermel model uses a semi-empirical relationship amongst the wind speed at flame height and terrain slope to produce fire spread. The fire and atmosphere are coupled by fire-generated heat and moisture fluxes which then perturb the lower atmospheric model layers via an exponential decay function with height (described in Clark et al., 1996a,b and Coen et al., 2013). The Rothermel model has known limitations in that it assumes a narrow, linear fire line and neglects key landscape-scale fire components such as spotting and mass fire (Andrews, 2018). It is hypothesized that these limitations play a role in the poorly developed plume structure seen in the control simulations (Shamsaei et al., 2023b). To bypass this deficiency, the Rothermel model is replaced by continuously updated fire perimeters derived from NEXRAD radar data. This technique is based on locating local maxima in the radar reflectivity and associated active combustion, and then aggregating these points into an evolving fire polygon (Lareau et al., 2022b). The process has been validated against infrared observations for several fires, including the Bear and Caldor fires. These radar perimeters are converted to a time-of-arrival grid that is passed into WRF-Fire, which controls the time at which a given cell in the fire mesh ignites. This process is similar to the satellite-based time-of-arrival approach used by Farguell et al. (2021). This "forced fire" approach maintains consistent fire rate and direction of spread across all of the sensitivity tests, allowing us to isolate the impact of fuel load on the heat fluxes and plume development without having to interpret changes in fire ROS, which itself is a function of fuel load in the Rothermel model.

3.4 Fuel Depiction and Fire Residence Time

The WRF-Fire simulations use the Scott and Burgan 40 (SB40) fuel categories (Scott and Burgan, 2005) derived from the LANDFIRE 2016 (Rollins, 2009) dataset to represent fuel type and load in the model domain. The LANDFIRE dataset is widely used among the wildfire modeling community because of its high resolution (30 x 30 m) coverage of fuel type, fuel load, fuel bed depth, and surface area to volume ratio across the contiguous United States (DeCastro et al., 2022). The dominant SB40 fuel category in the central Sierra Nevada is Timber-Understory 5 (TU5), comprising 69% and 73% of the simulated burn area in the Bear and Caldor Fires, respectively (Fig. 4). The TU5 fuel type is a high-load conifer litter and shrub understory with a combined 1-, 10-, and 100-hour fuel load of 2.47 kg m^{-2} (11 t ac^{-1}) and moderate flame length and spread rate (Scott and Burgan, 2005).

This default fuel load of ~2.5 kg m^{-2}, however, is a drastic underestimate of the fuels available-for and consumed-in large fires, especially fuels consumed after the passage of the initial fire front. For example, using pre- and post-fire fuel measurements in in the central Sierra Nevada, Cansler et al. (2019) found an average fuel consumption of 15.1 kg m^{-2}(151 Mg ha^{-1}) during the 2013 Rim Fire in Yosemite National Park. Similarly, McCarley et al. (2020) showed airborne laser scanning estimated fuel consumption in large wildfires exceeding 20 kg m^{-2} (200 Mg ha^{-1}) over large areal expanses. These observations suggest that, even in the best-case simulations with WRF-Fire and SB40 fuels, fires may not yield total released heat comparable to those in real fires, and thus cannot simulate the strong fire-generated circulations (e.g., updrafts

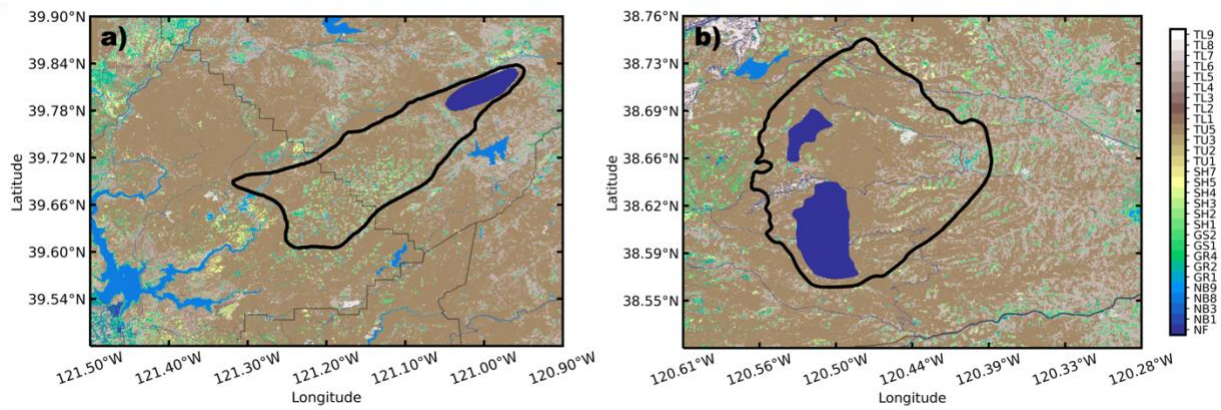

Figure 4. SB40 fuel category map for the (a) Bear Fire and (b) Caldor Fire. Dark blue no fuel (NF) region shows estimated initial perimeter used to initiate WRF-Fire simulation with final fire perimeter shown in black.

Table 2. Summary of case studies and variables.

Case Name	TU5 Fuel Load (kg m^{-2})	w	Fuel Moisture (%)	Fire Spread Method
BearControl	2.47	900	5	Rothermel
BearFuelx1	2.47	4080	5	NEXRAD
BearFuelx4	9.86	4080	5	NEXRAD
BearFuelx8	19.73	4080	5	NEXRAD
CaldorControl	2.47	900	5	Rothermel
CaldorFuelx1	2.47	3825	5	NEXRAD
CaldorFuelx4	9.86	3825	5	NEXRAD
CaldorFuelx8	19.73	3825	5	NEXRAD

and inflows) that feedback on fire processes. This deficiency is apparent in Figure 1 when comparing the preliminary simulation (Fig. 1c,d) to observed flow perturbations (Fig. 1a,b).

To examine the sensitivity of fire-generated circulations to fuel loads we devise three sensitivity tests all using the same observationally-based prescribed fire spread. Due to the dominance of TU5 fuels in the study area, and to eliminate further uncertainties in fuel types, only the TU5 fuel loads are adjusted in this study. We first use a control case with the default TU5 load of 2.47 kg m^{-2} (Fuelx1) and two augmented fuel loads of 9.86 kg m^{-2} (Fuelx4) and 19.73 kg m^{-2} (Fuelx8) (Table 2). Note that the Fuelx8 cases are similar to observed loads and consumption of 15-20 kg m^{-2} described above, and thus a priori we expect these simulations to best match observations.

In addition to the fuel load, in WRF-Fire each SB40 fuel category has a weighting parameter controlling the fire's residence time. This weighting factor is defined as

$$w = 0.8514 \times T_f \,, \tag{1}$$

where T_f is the time for the fuel to burn down to $e^{-1} \approx 0.3689$ of the initial fuel load (Mandel et al., 2011). The default values for w are derived from approximations of mass-loss curves from the Albini and Reinhardt (1995) BURNUP algorithm (Clark et al., 2004); however, Mandel et al. (2011) noted there is significant uncertainty in the default values used in WRF-Fire. Due to the relationship between fuel load and burnout time, w must proportionally change with fuel loads to avoid unphysically large heat release rates (i.e. burning the fuel too quickly) under increased fuel scenarios. The value of w also impacts the breadth of the combusting region: for a given fuel load a larger w produces a broader combusting region when we force the perimeters to observations, and thus constrain the rate of spread. We note that, when using the Rothermel spread model after increasing the fuel load and the weighting parameter, the fire spread unrealistically decreases, thus highlighting the need for forced fire perimeter approach in the sensitivity analyses.

Since the values of w used in WRF-Fire are uncertain, we use GOES-17 Fire Radiative Power (FRP) data to estimate representative values for T_f (burnout time) and thus w using the relationship shown by Eq. 1 from Mandel et al. (2011). The FRP algorithm uses the 3.9 µm and 11.2 µm brightness temperatures along with a number of temporal and spatial checks to characterize fire temperature, size, and FRP and is thus a useful metric in identifying regions of active fire (Schmidt et al., 2012) and how long fire resides within a given pixel (2 km x 2 km). We estimate this "pixel" residence time by evaluating each GOES-17 pixel during the simulation timeframe (Table 1) to determine when the pixel reached maximum FRP (Fig. 5). Then, we evaluated how long each pixel took to cool to e^{-1} of its normalized FRP maxima and defined the value as T_f (interquartile ranges for all pixels depicted with red shading in Fig. 5). Individual pixel T_f values are shown in the insets of Fig. 5 for both the Bear (Fig. 5a) and Caldor (Fig. 5b) Fires. We note that the pixel residence time is not purely the physical burndown time of the fuels since it includes information about both the rate of spread through the pixel and the consumption of fuel. Nonetheless, it is a useful approach for grounding our simulations in an observational framework. T_f values for all fire pixels during the timeframe are then averaged (maroon line in Fig. 5) to produce a representative T_f and w value for each fire. The resulting analysis suggests values of 4080 and 3825 seconds are appropriate for the Bear (Fig. 5a) and Caldor (Fig. 5b) fires, respectively, which is about four times larger than the default value in WRF-Fire (900 s). These w values are not intended to be physical or universal for improving freely evolving WRF-Fire simulations, but rather an approach at producing realistic breadth of the combusting zone for the given cases using the forced fire perimeters, described below.

3.5 Radar Observations of Plume Processes

In addition to providing estimated fire perimeters, NEXRAD radar data are also used to compare simulated fire-generated circulations with observed plume injection heights and fire-generated flows. Specifically, we use radar reflectivity and radial velocity cross sections extracted from a cartesian gridded version of the NEXRAD observations (see Lareau et al., 2022a) to document plume structure, plume injection height, and radial wind components due to the ambient and fire-generated winds. These data provide a useful validation approach for landscape scale fires where in-situ measurements are otherwise unavailable (e.g., Jones et al. 2022).

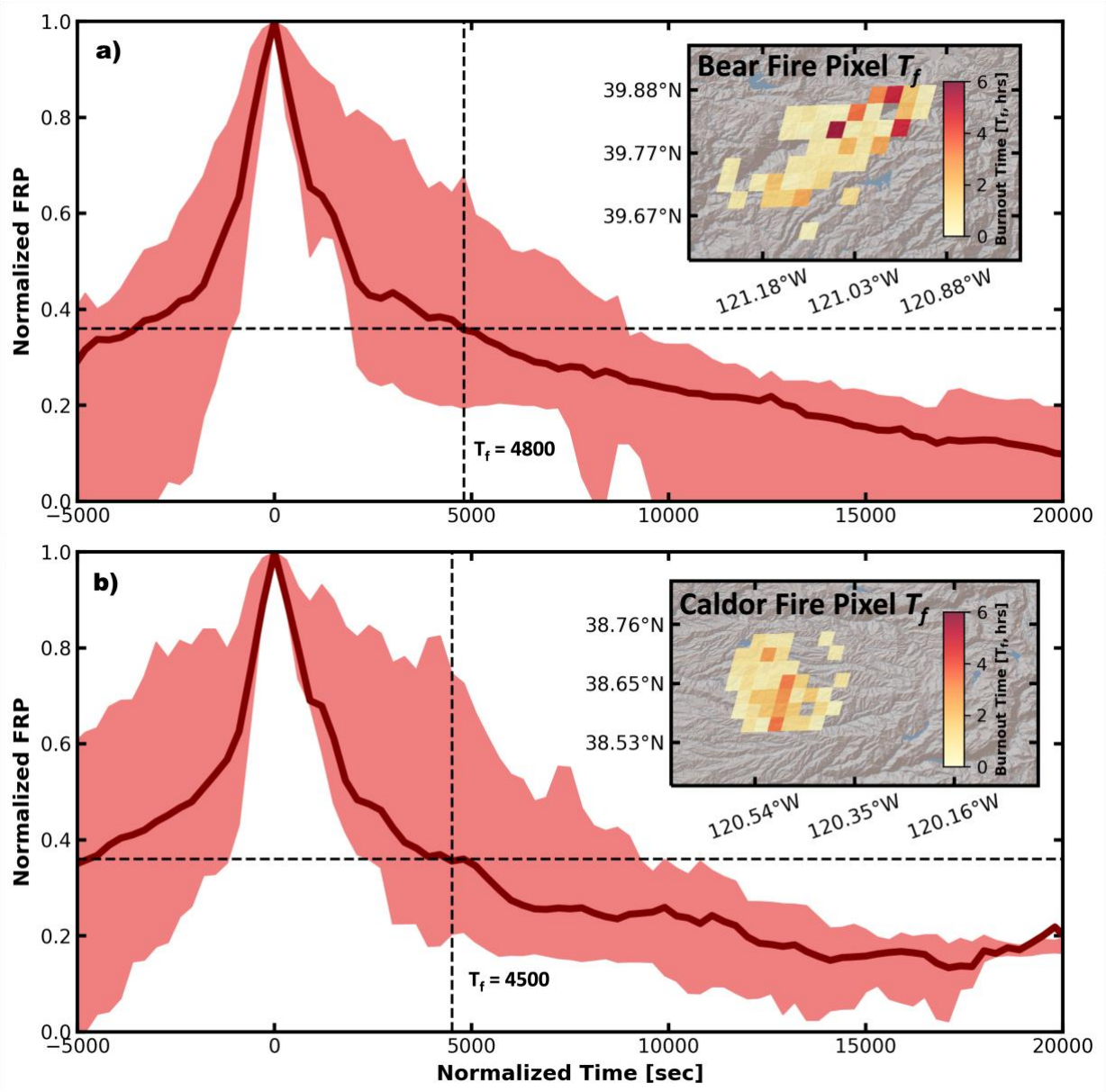

Figure 5. Fire-averaged FRP timeseries (maroon line) and interquartile ranges (light red shading) of individual pixel FRP normalized by maximum detected FRP in the scene. Pixel T_f (inset, shaded) for the (a) Bear Fire and (b) Caldor Fire. Horizontal black dashed line indicates e^{-1} of normalized FRP, and vertical dashed black line indicates Tf where average FRP crosses e^{-1}.

257

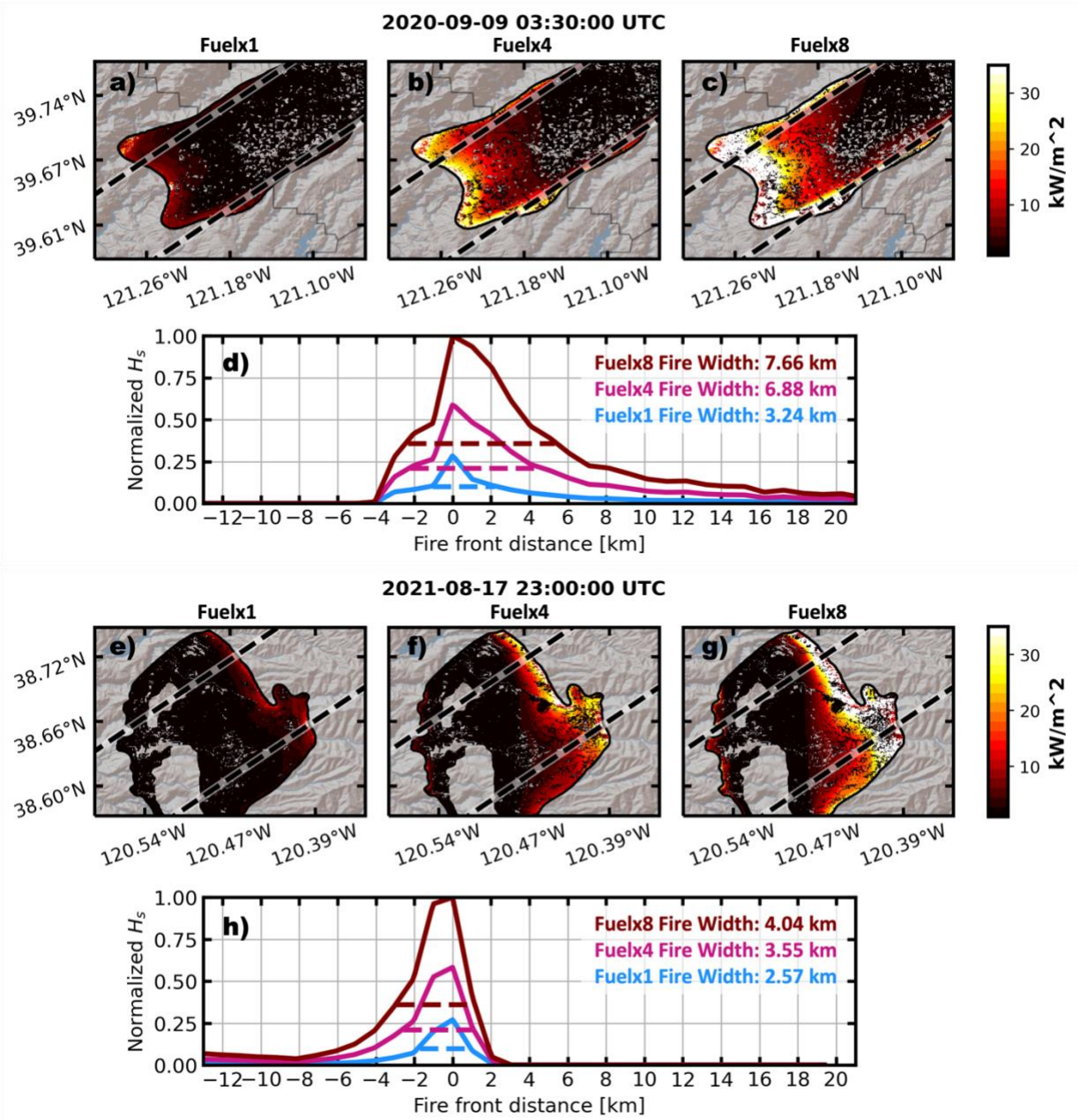

Figure 6. Fire generated heat flux for the (a-c) Bear Fire and (e-g) Caldor Fire. Normalized cross sections of fire heat flux with fire width indicated by dashed line at e^{-1} of the peak heat release for the Fuelx1 (light blue), Fuelx4 (magenta), and Fuelx8 (maroon) scenarios for the (d) Bear and (h) Caldor Fires.

258

4 Results

4.1 Fireline Width and Intensity

Our simulations show that increasing TU5 fuel loads and burnout timescale (T_f) while forcing the fire spread increases the areal extent and width of intense (>10 kW m^{-2}) fire-generated sensible heat fluxes for both the Bear and Caldor fires (Fig. 6). To quantify these changes, we use an e-folding scale (e.g., ~0.37) of the peak fire-generated sensible heat flux to identify the width of the head fire (see dashed lines in Fig. 6d, h) in each simulation, where "fire front distance" corresponds to the horizontal distance from the normalized maximum heat flux in the head fire region.

The results show that at 330 UTC the Bear Fire Fuelx1 scenario generates a narrow (~3.2 km, Fig. 6d) head fire with a maximum sensible heat flux of ~9 kW m^{-2} (Fig. 6a) whereas the Fuelx4 scenario has a comparatively wider (~6.9 km, Fig. 6d) head fire with a maximum of 34 kW m^{-2} (Fig. 6b). Finally, the Fuelx8 scenario produces the widest (~7.7 km, Fig. 6d) head fire with a peak sensible heat flux of 68 kW m^{-2} (Fig. 6c). Heat fluxes of this magnitude are consistent with those estimated in recent observational studies of plume rise (e.g., Lareau and Clements, 2017).

Similar changes in the head fire width and heat fluxes are simulated for the Caldor Fire. Specifically, at 2300 UTC, the Caldor Fuelx1 scenario produces a relatively narrow (~2.6 km, Fig. 6h) head fire with a maximum heat flux of ~9 kW m^{-2} (Fig. 6e), whereas the Fuelx4 scenario has a head fire width of ~3.6 km (Fig. 6h) with a peak heat flux of ~36 kW m^{-2} (Fig. 6f), and the Fuelx8 scenario has the widest fire head (~4 km, Fig. 6h) and highest maximum fire heat flux (~73 kW m^{-2}, Fig. 6g).

These results show that increasing the fuel load and weighting factor increases the maximum fire-generated heat flux and the areal extent of the head fire, thus implying a wider "flaming region" that better agrees with available infrared (e.g., GOES-17) observations (Fig. 7). For example, Fig. 7 shows down-sampled versions of the WRF-Fire sensible heat fluxes to mimic the GOES-17 FRP satellite footprint (2x2km). For this comparison the FRP data are converted to sensible heat fluxes using the assumption that FRP is approximately one tenth the sensible heat flux (Val Martin et al., 2012). We note that there is uncertainty in these measurements due to sensor saturation and shading from pyroCb, likely resulting in artificially low observed intensities. Nonetheless, these comparisons show that both the Bear and Caldor Fire Fuelx8 (Fig. 7d,h) simulations compare favorably with the observations (Fig. 7a,e), whereas the Fuelx1 (Fig. 7b,f) and Fuelx4 (Fig. 7c,g) cases insufficiently represent the breadth of intense combustion. As we show in the next two sections, only the simulations with wider and higher intensity combustion zones yield atmospheric response comparable to the observations.

4.2 Fire-Generated Horizontal Flow Perturbations

Commensurate with the changes in fire heat flux and head fire width, our simulations show improved representation of the fire-generated horizontal flow perturbations with increasing fuel loads. The horizontal component of the flow is evaluated by comparing "radial velocity" observations from the NEXRAD radar with the flow component in the simulations that would be observed with a hypothetical radar in the same location. This is accomplished by computing the component of the simulated winds that projects onto radials originating from the radar base locations (KBBX and KDAX for the Bear and Caldor Fires, respectively), and thus provide a

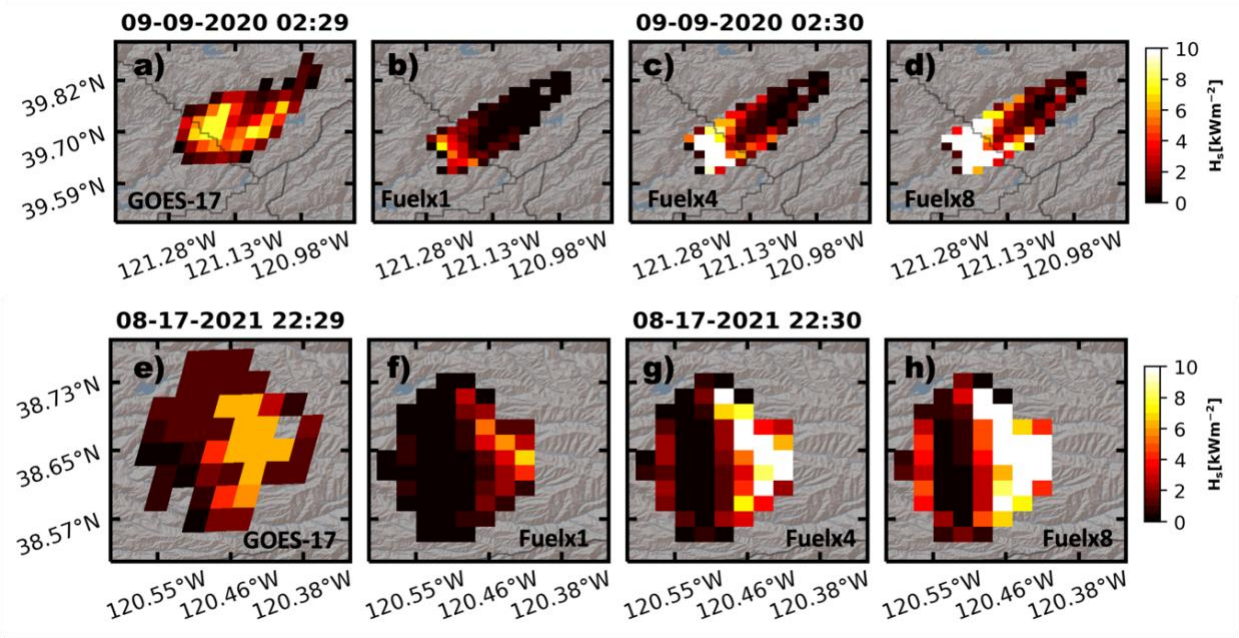

Figure 7. Observed GOES fire intensity using FRP converted to sensible heat flux for the (a) Bear Fire and (e) Caldor Fire. WRF-Fire sensible heat flux for the (b-d) Bear and (f-h) Caldor Fires. WRF-Fire sensible heat fluxes are down-sampled to a 2x2 km grid to emulate the GOES FRP data resolution.

direct comparison with the wind components observed by the radars. In this framework, all winds are either "inbound" (shown in blue) or "outbound" (shown in red) relative to the radar location.

For the Bear Fire, the observed radial velocities from the KBBX NEXRAD on 9 September 2020 at 330 UTC indicate strong downslope winds of ~25 m s^{-1} towards the radar (blue shading and white arrows, Fig. 8a, b), with a pronounced region of flow reversal in the lee of the fire head indicated by outbound radial velocities of 5-10 m s^{-1} (red shading and black arrows, Fig. 8a, b). The flow reversal is clear observational evidence for a mesoscale fire-generated wind that produces strong convergence at the fire front and feeds the vigorous fire-generated updrafts. While all three fuel scenarios depict strong, downslope winds and inbound radial velocities greater than 20 m s^{-1} (Fig. 8c-h), they differ in the magnitude and extent of the fire-generated flow reversal. The Fuelx1 scenario shows no flow reversal, with inbound radial velocities of 20-25 m s^{-1} spanning the fire head (Fig. 8c,d) and no evidence of feedback from the fire (e.g., no flow weakening or reversal to the west of the fire head), which is clearly deficient. The Fuelx4 scenario has a small region of near-zero to slightly positive radial velocities west of the fire head (Fig. 8e,f). The Fuelx8 scenario has the greatest extent of outbound radial velocities in the lee of the head fire and covering a greater areal extent than the Fuelx4 scenario (Fig. 8g, h). This area of positive (5-8 m s^{-1}) radial velocities is around 2 km MSL with small regions of stagnant flow extending up to 3 km MSL. Strong negative radial velocities upwind of fire front indicate a region of strong convergence with the fire-generated wind at the head fire. While the Fuelx8 scenario is in best agreement with the observations, it still underestimates the strength and spatial extent of the fire-generated winds apparent in the

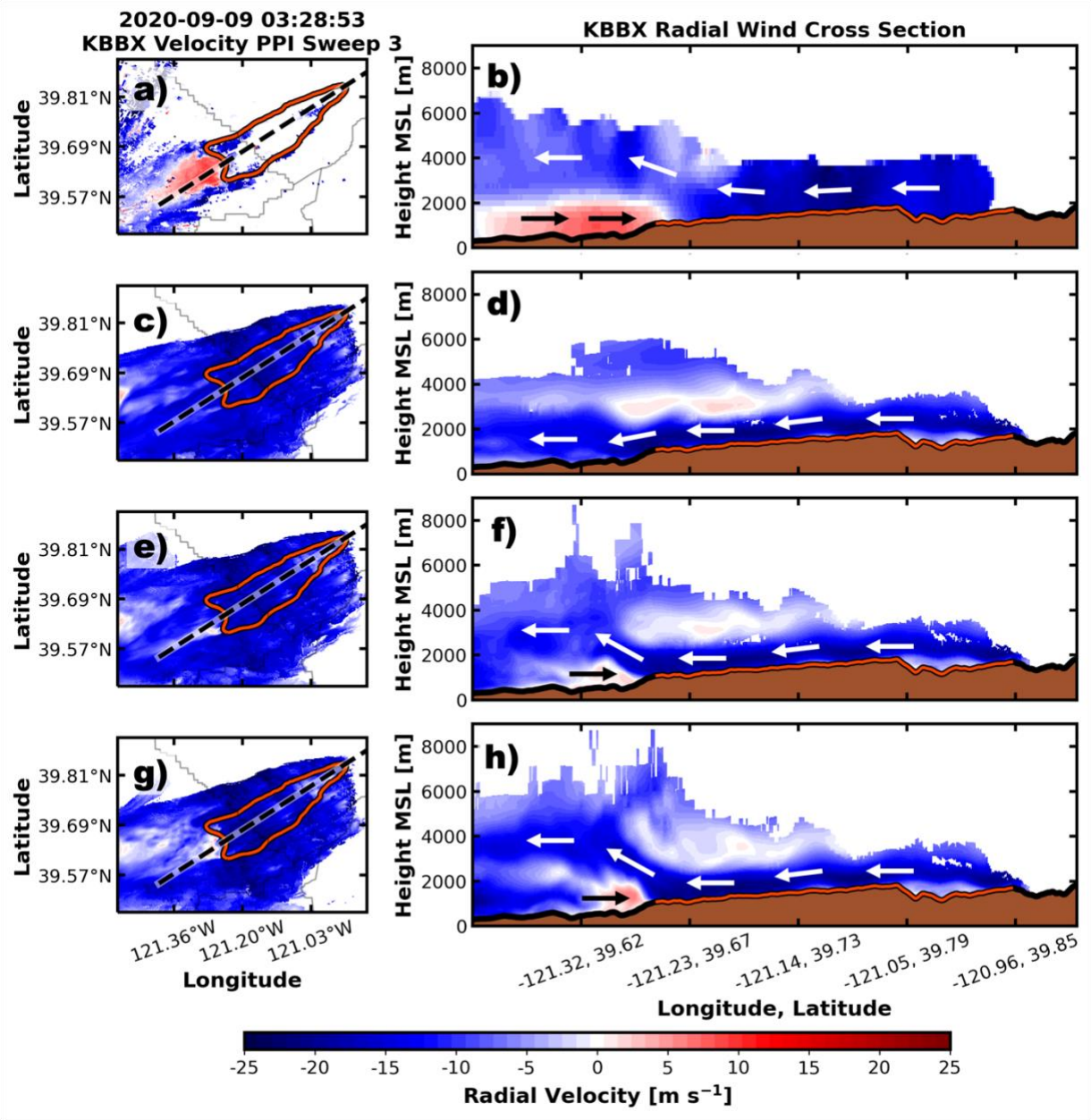

Figure 8. Comparison of observed and simulated fire flows during the Bear Fire. (a) Beale Air Force Base (KBBX) NEXRAD radial velocity PPI (shaded) and radar-estimated fire perimeter (red contour), (b) radial wind and radar-estimated fire perimeter (red line) cross section along black dashed line, WRF-Fire simulated PPI and cross section of in-plume radial velocity and fire perimeter for (c-d) Fuelx1, (e-f) Fuelx4, and (g-h) Fuelx8 scenarios, around 0330 UTC September 9, 2020. In-plane directional flow vectors annotated in b, d, f, h.

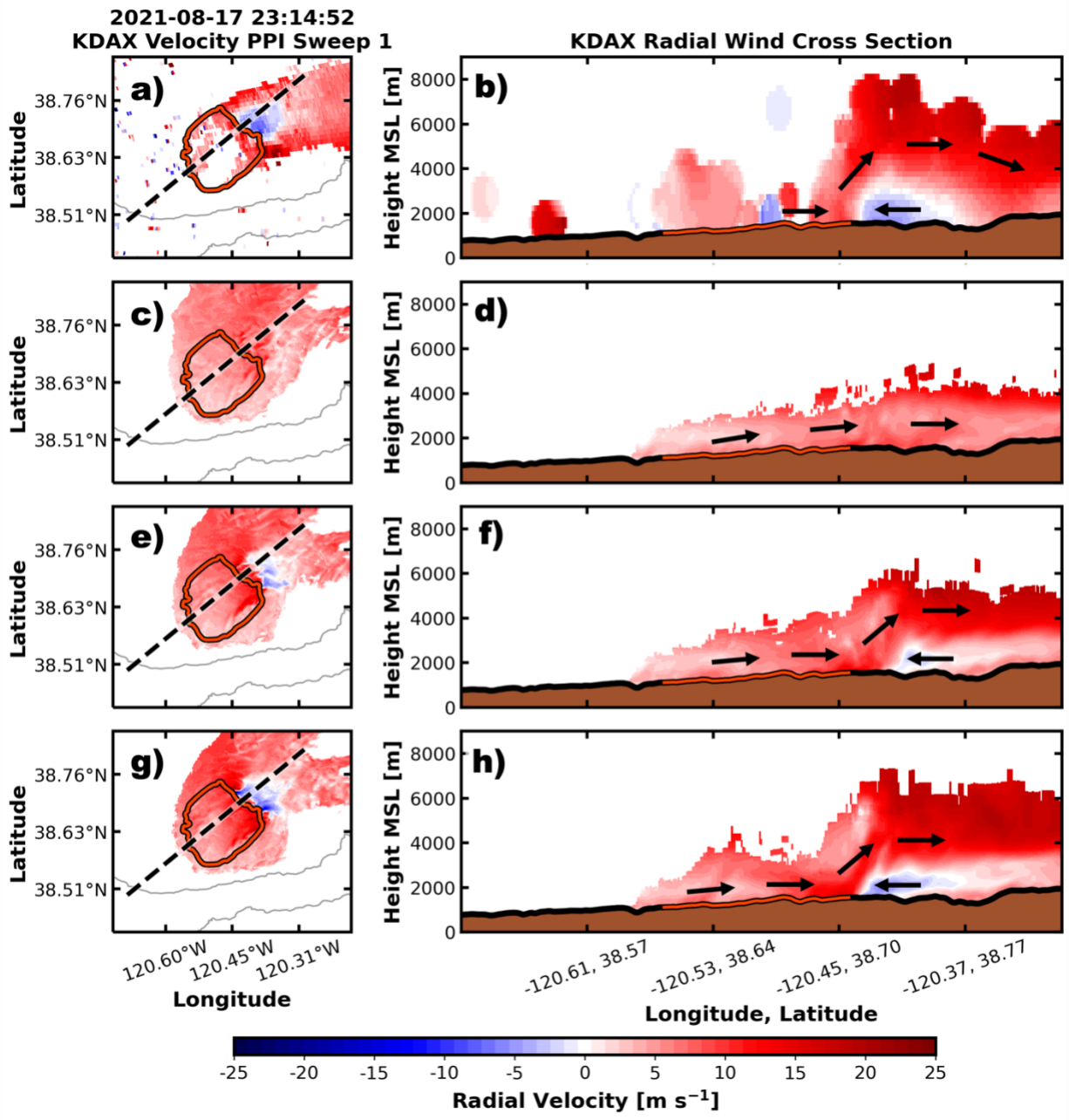

Figure 9. Comparison of observed and simulated fire flows during the Caldor Fire. (a) Sacramento (KDAX) NEXRAD radial velocity PPI (shaded) and radar-estimated fire perimeter (red contour), (b) radial wind and radar-estimated fire perimeter (red line) cross section along black dashed line, WRF-Fire simulated PPI and cross section of in-plume radial velocity and fire perimeter for (c-d) Fuelx1, (e-f) Fuelx4, and (g-h) Fuelx8 scenarios, around 2315 UTC August 17, 2021. In-plane directional flow vectors annotated in b, d, f, h.

observations, suggesting that the actual fuel consumption, or rate of consumption, during the Bear Fire may exceed our simulated results.

We find similar sensitivity to fire-generated horizontal winds for the Caldor Fire when we compare simulated radial velocities with those observed by the Sacramento NEXRAD (KDAX) on 17 August 2021 around 2315 UTC. To be specific, the observations indicate upslope flow with generally positive (outbound) background radial velocities of around 10 m s^{-1} (red shading in Fig. 9a, b) with a pronounced region of fire induced flow reversal (inbound, blue shading) radial velocities in the lee of the fire head that extends up to approximately 4 km MSL. Similar to the Bear Fire, the Caldor Fuelx1 scenario shows no evidence of fire generated flow reversal, with positive radial velocities of 5-10 m s^{-1} extending across the fire front, and no region of flow weakening or reversal near the fire head (Fig. 9c,d). The Fuelx4 scenario shows a small region of stagnant to negative radial velocities (0-5 m s^{-1}) on the northeast lobe of the fire head (Fig. 9e). Fig. 9f shows this region of inbound radial velocities extends up to about 3 km MSL and is slightly displaced downstream of the fire head. The Fuelx8 scenario again shows the most pronounced flow perturbation by the fire with a larger region of inbound radial velocities in the lee of the fire front with peak values around 10 m s^{-1} (Fig. 9g). Fig. 9h shows the maximum of this flow reversal region is situated immediately downstream of the fire front, with flow stagnation extending well downstream of the fire head as evidenced by the region of weakly positive radial velocities.

A clear takeaway from these results is that when models produce too little heat flux, they also produce deficient fire-generated horizontal winds and thus do not capture critical components of the feedback between the fire and the atmosphere. In that these fire-generated winds have been identified as contributors to the onset of extreme events, such as FGTVs (Lareau et al., 2022a), this data deficiency urgently needs to be resolved.

4.3 Plume Depth and Updraft Strength

Consistent with the increase in horizontal flow perturbations, our simulations also show increases in vertical velocity, plume verticality, pyroCu/Cb initiation, and smoke injection height which are proportional to the increase in fuel load and thus heat flux (Fig. 10a-c).

To frame the simulation results, we first examine radar observations of the plume structure. During the Bear Fire, representative radar cross sections indicate an upright plume core (e.g., corridor of high reflectivity) rising from the head fire with plume tops near 9 km MSL (Fig. 10d). Further analysis of the plume evolution from 0000-0300 UTC (not shown, see also Lareau et al., 2022a,b) indicates plume tops ranging from 8 to almost 12 km MSL including considerable pyroCu/Cb development, with cloud bases near 6 km MSL. While we do not have updraft observations, it is reasonable to conclude that these deep, nearly vertical plume cores must possess very strong (e.g., >30 m s^{-1}) updrafts that can compete with the strong cross flow (25-30 m s^{-1}) to produce an upright plume core.

Unsurprisingly, these upright plume structures and high vertical velocities are absent from the Fuelx1 simulations, but present in the high fuel load cases (Fig. 10a-c). To be specific, at 0200 UTC in the Bear Fire Fuelx1 simulation, maximum updraft velocities are less than 10 m s^{-1} and do not penetrate above 3 km MSL (Fig. 10a). The maximum smoke plume depth in this scenario is less than 4 km MSL. The Fuelx4 simulation has maximum updraft velocities of just over 20 m s^{-1} with comparatively wider and deeper updraft cores of ~3 km wide and 5-6 km MSL deep, respectively (Fig. 10b). The smoke plume depth reaches 6 km MSL in this scenario,

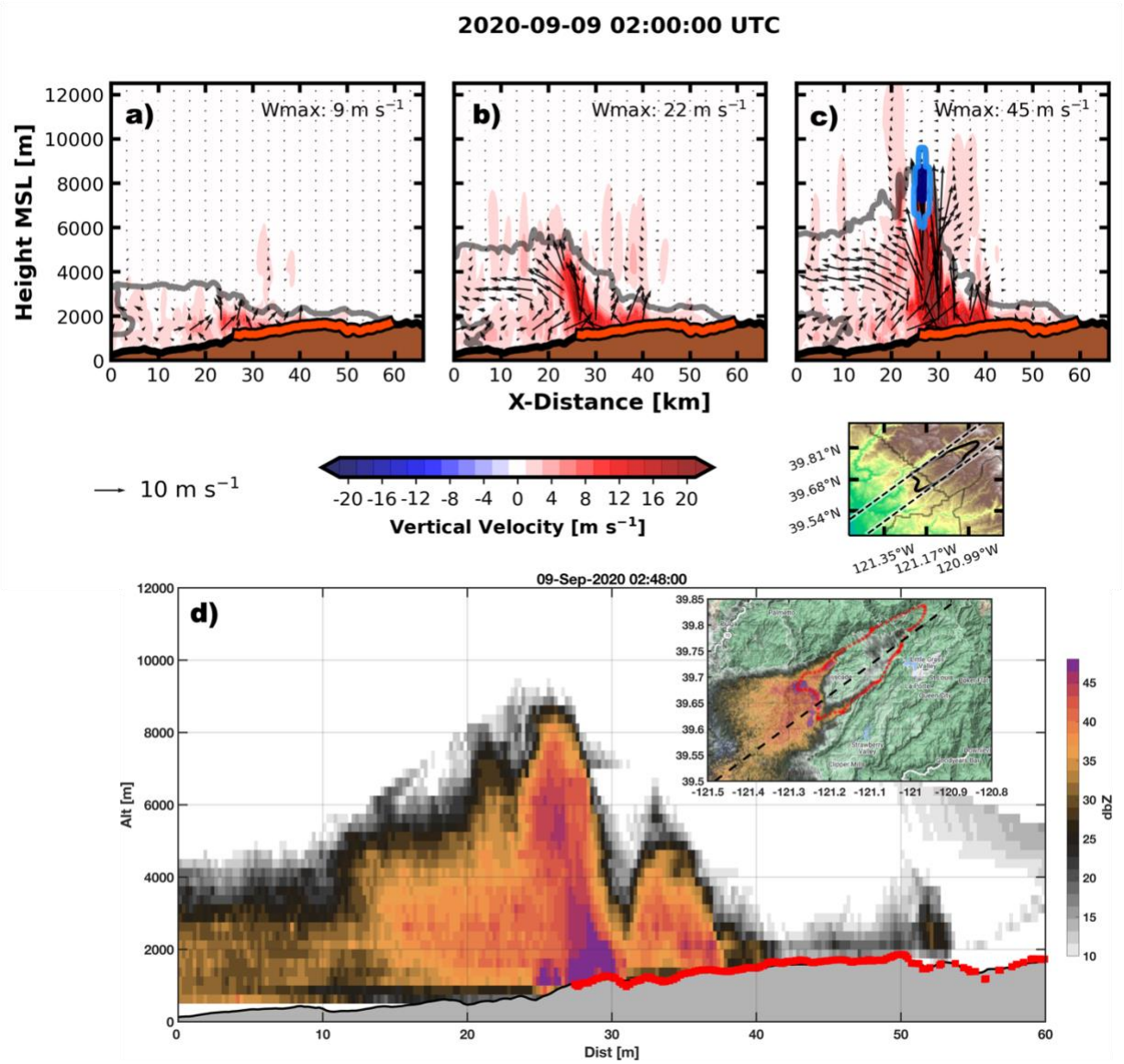

Figure 10. Bulk cross section normal to the Bear Fire head of fire-generated maximum vertical velocity (shaded), in-plane average fire-generated wind vectors, smoke plume extent (gray contour), cloud water (navy) and ice (light blue) contours in the (a) Fuelx1, (b) Fuelx4, and (c) Fuelx8 simulations, and (d) observed NEXRAD reflectivity (shaded) cross-section.

and a fire-generated circulation is evident in the lee of the plume with surface inflow, and outflow at about 3-4 km MSL. The Fuelx8 simulation has the deepest, strongest, and most upright plume of any scenario with vertical velocities exceeding 40 m s^{-1} and penetrating to 8-10 km MSL (Fig. 10c). The wide (~5km) updraft base is inducing strong inflow at the surface and strong outflow at 4-6 km MSL in the lee of the plume. Notably, this scenario produced multiple instances of pyroCb, with a high-based pyroCb occurring at 0200 UTC between 6 and 10 km MSL (see blue cloud water contour in Fig. 10c), consistent with NEXRAD and photographic observations during this period (Fig. 10d, see also Fig. 10 in Lareau et al., 2022a). The strong

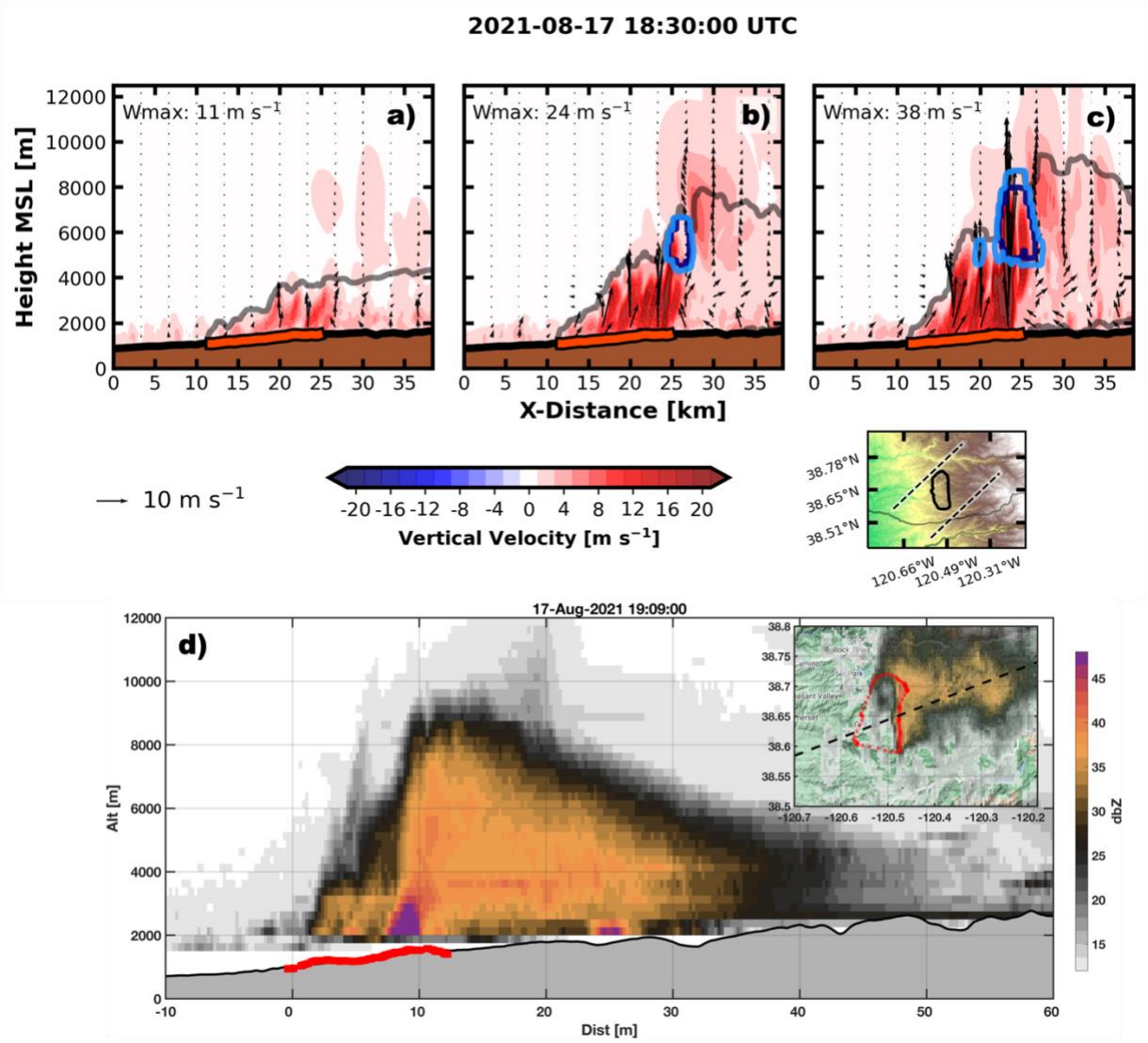

Figure 11. Bulk cross section normal to the Caldor Fire head of fire-generated maximum vertical velocity (shaded), in-plane average fire-generated wind vectors, smoke plume extent (gray contour), cloud water (navy) and ice (light blue) contours in the (a) Fuelx1, (b) Fuelx4, and (c) Fuelx8 simulations, and (d) observed NEXRAD reflectivity (shaded) cross-section.

simulated updrafts linked to pyroCb are consistent with observations of other extreme wildfires (Rodriguez et al. 2020).

Whereas the Bear Fire updrafts must compete with very strong ambient winds, the Caldor Fire's updrafts experience much weaker background flow yet show similar sensitivity to fuel load. For example, at 1830 UTC, the Caldor Fire Fuelx1 simulation (Fig. 11a) produces maximum updrafts of ~10 m s^{-1} reaching ~4 km MSL with ill-defined updraft cores. The Fuelx4 simulation (Fig. 11b) produces updraft velocities greater than 20 m s^{-1}, penetrating up to ~5 km MSL and producing shallow pyroCu between 5 and 7 km MSL. This scenario contains a comparatively wide (~10 km) updraft region containing several narrow updraft cores from the surface up to 5 km MSL. There is also a weak fire induced circulation in the lee of the plume,

with weak surface inflow vectors and slightly stronger outflow at about 3-4 km MSL. The Fuelx8 scenario (Fig. 11c) contains the most coherent updrafts with a ~5 km wide and ~8 km MSL deep region of vertical velocities just under 40 m s^{-1}. The resulting plume depth in this scenario neared 10 km, with a 4-5 km deep pyroCu/Cb, well-developed surface inflow region, and ~4km MSL outflow in the lee of the plume. This simulated plume and pyroCu/Cb structure compares well with the KDAX NEXRAD data, where plume tops were around 10 km MSL (Fig. 11d) and high reflectivity cores suggest upright and vigorous updrafts.

The results of both the Bear Fire and Caldor Fire simulations indicate that not only are fuel characteristics important in generating realistic plumes and fire-generated flows, but they also have clear implications for simulating deep pyroCb, which can generate additional feedbacks on the fire environment (e.g., downdrafts, lightning, FGTVs) and may result in stratospheric smoke injection.

5 Summary and Discussion

Our sensitivity analyses indicate that WRF-Fire run with Scott and Burgen 40 fuel categories under-represents fuel quantity and its consumption, and thus underrepresents fire-generated heat fluxes, resulting in deficient simulation of the atmospheric response to landscape-scale wildfire processes. Among these deficiencies are shallow plumes with weak updrafts and little-to-no fire-induced flow perturbations. These deficiencies are also driven by insufficiently wide areas of combustion behind the fire-front (e.g., "deep flaming" in the model), which is linked to both the deficient fuel load and the fire's residence time. For example, neither the Bear nor Caldor Fire baseline (Fuelx1) simulations produced a broad combustion region with sufficiently large sensible heat fluxes to produce deep updrafts initiating pyroCu/Cb. This stands in stark contrast to radar observations of both fires, which reveal deep, upright convective cores linked to pyroCu/Cb. In contrast, the Fuelx4 and Fuelx8 scenarios generated wider combustion zones and greater total heat fluxes resulting in deep (e.g., 10 km MSL) upright plumes with vigorous updrafts initiating pyroCu/Cb. Since strong inflows, updrafts, and pyroCu/Cb initiation are all vital mechanisms for the development of extreme fire behavior (e.g., FGTVs, long-range spotting) this sensitivity to fuel load underscores current shortcomings in the fuel inputs driving WRF-Fire. Such shortcomings likely apply to other coupled fire-atmosphere models using the Rothermel spread model combined with LANDFIRE-informed fuel data sets (such as Anderson 13 or SB40), ultimately limiting their capacity to accurately simulate landscape-scale fires.

While some efforts have been made to improve this representation by adjusting fuel categories via machine learning (DeCastro et al., 2022) and accounting for canopy fuels through addition of crown fire heat and improved heat release schemes (Shamsaei et al., 2023b), the foundation of both the Anderson 13 and SB40 fuel data is surface fuels in LANDFIRE which appears to severely underrepresent real-world fuel loads available for consumption in large fires. Such fuel availability is directly linked to wildfire energy release (Goodwin et al., 2021). Thus for accurate, operational simulations of landscape scale fire spread, a methodology that incorporates both surface and canopy fuel loading (e.g., dead and down debris, standing dead, etc.) and landscape-scale fire processes (e.g., spotting, mass-fire, post-frontal combustion) must be incorporated into coupled fire-atmosphere models.

In identifying these shortcomings, a potential path forward involves improved representation of fuel inputs (e.g., inclusion of canopy and down woody fuel loading in LANDFIRE) for use in WRF-Fire and other coupled fire-atmosphere models. However, in our

simulations we bypassed the large uncertainties in fire spread due to fuel loading by forcing the fire perimeter with observations. This enabled us to change the fuel loads without changing the rate of spread. In freely evolving simulations this is not possible, and simply increasing the fuel load will yield, by formulation, slower rate of spread from the Rothermel model. This issue is compounded in that our forced perimeters include the result of near- and long-range spotting whereas the Rothermel model does not represent long-range spotting. Thus, to achieve high fidelity and freely evolving simulations critical for operational forecasting, the community will need to improve the underlying physical representation of fire spread processes, not just the fuel and its consumption. In the meantime, a combination of assimilating fire perimeter observations (e.g., Farguell et al., 2021 and the approach used herein) and adjusting fuel loads based on machine learning is one approach to bypass uncertainties in the model physics and realize potentially useful simulations not just of the fire spread but also the attendant atmospheric circulations.

Acknowledgments

Funding for this work is provided through the National Science Foundation's Leading Engineering for America's Prosperity, Health, and Infrastructure (LEAP-HI) program by grant number CMMI-1953333. We would like to acknowledge high-performance computing support from Cheyenne (doi:10.5065/D6RX99HX) provided by NCAR's Computational and Information Systems Laboratory, sponsored by the National Science Foundation. The National Center for Atmospheric Research is a major facility sponsored by the National Science Foundation under Cooperative Agreement 1852977. The authors declare no conflicts of interest relevant to this study.

Data Availability Statement

WRF-Fire output was analyzed using Python 3.8. Model output, processing codes, and fire perimeter files (https://doi.org/10.7910/DVN/FEHPIH; Roberts and Lareau, 2023) are available on Harvard Dataverse. Ancillary data used in these analyses are free and publicly available through AWS. NEXRAD and GOES-17 data are available at https://registry.opendata.aws/noaa-nexrad/ and https://registry.opendata.aws/noaa-goes/.

References

Albini, F., & Reinhardt, E. (1995). Modeling Ignition and Burning Rate of Large Woody Natural Fuels. *International Journal of Wildland Fire*, *5*(2), 81. https://doi.org/10.1071/WF9950081

Andrews, P. L. (2018). *The Rothermel surface fire spread model and associated developments: A comprehensive explanation* (No. RMRS-GTR-371) (p. RMRS-GTR-371). Ft. Collins, CO: U.S. Department of Agriculture, Forest Service, Rocky Mountain Research Station. https://doi.org/10.2737/RMRS-GTR-371

CalFire Incident Archive. (2021). *Caldor Fire*. Retrieved from https://www.fire.ca.gov/incidents/2021/8/14/caldor-fire

Chen, F., & Dudhia, J. (2001). Coupling an Advanced Land Surface–Hydrology Model with the Penn State–NCAR MM5 Modeling System. Part I: Model Implementation and Sensitivity. *Monthly Weather Review*, *129*(4), 569–585. https://doi.org/10.1175/1520-0493(2001)129<0569:CAALSH>2.0.CO;2

Clark, T., Jenkins, M., Coen, J., & Packham, D. (1996a). A Coupled Atmosphere-Fire Model: Role of the Convective Froude Number and Dynamic Fingering at the Fireline. *International Journal of Wildland Fire*, *6*(4), 177. https://doi.org/10.1071/WF9960177

Clark, T. L., Jenkins, M. A., Coen, J., & Packham, D. (1996b). A Coupled AtmosphereFire Model: Convective Feedback on Fire-Line Dynamics. *Journal of Applied Meteorology*, *35*(6), 875–901. https://doi.org/10.1175/1520-0450(1996)035<0875:ACAMCF>2.0.CO;2

Clark, T. L., Coen, J., & Latham, D. (2004). Description of a coupled atmosphere - fire model. *International Journal of Wildland Fire*, *13*(1), 49. https://doi.org/10.1071/WF03043

Coen, J. L., Cameron, M., Michalakes, J., Patton, E. G., Riggan, P. J., & Yedinak, K. M. (2013). WRF-Fire: Coupled Weather–Wildland Fire Modeling with the Weather Research and Forecasting Model. *Journal of Applied Meteorology and Climatology*, *52*(1), 16–38. https://doi.org/10.1175/JAMC-D-12-023.1

Coen, J. L., Stavros, E. N., & Fites-Kaufman, J. A. (2018). Deconstructing the King megafire. *Ecological Applications*, *28*(6), 1565–1580. https://doi.org/10.1002/eap.1752

Deardorff, J. W. (1980). Stratocumulus-capped mixed layers derived from a three-dimensional model. *Boundary-Layer Meteorology*, *18*(4), 495–527. https://doi.org/10.1007/BF00119502

DeCastro, A. L., Juliano, T. W., Kosović, B., Ebrahimian, H., & Balch, J. K. (2022). A Computationally Efficient Method for Updating Fuel Inputs for Wildfire Behavior Models Using Sentinel Imagery and Random Forest Classification. *Remote Sensing*, *14*(6), 1447. https://doi.org/10.3390/rs14061447

Dowdy, A. J., Ye, H., Pepler, A., Thatcher, M., Osbrough, S. L., Evans, J. P., et al. (2019). Future changes in extreme weather and pyroconvection risk factors for Australian wildfires. *Scientific Reports*, *9*(1), 10073. https://doi.org/10.1038/s41598-019-46362-x

Dudhia, J. (1989). Numerical Study of Convection Observed during the Winter Monsoon Experiment Using a Mesoscale Two-Dimensional Model. *Journal of the Atmospheric Sciences*, *46*(20), 3077–3107. https://doi.org/10.1175/1520-0469(1989)046<3077:NSOCOD>2.0.CO;2

Farguell, A., Mandel, J., Haley, J., Mallia, D. V., Kochanski, A., & Hilburn, K. (2021). Machine Learning Estimation of Fire Arrival Time from Level-2 Active Fires Satellite Data. *Remote Sensing*, *13*(11), 2203. https://doi.org/10.3390/rs13112203

Farr, T. G., & Kobrick, M. (2000). Shuttle radar topography mission produces a wealth of data. *Eos, Transactions American Geophysical Union*, *81*(48), 583. https://doi.org/10.1029/EO081i048p00583

Finney, M. A., & McAllister, S. S. (2011). A Review of Fire Interactions and Mass Fires. *Journal of Combustion, 2011*, 1–14. https://doi.org/10.1155/2011/548328

Goodwin, M. J., Zald, H. S. J., North, M. P., & Hurteau, M. D. (2021). Climate-driven tree mortality and fuel aridity increase wildfire's potential heat flux. *Geophysical Research Letters*, *48*, e2021GL094954. https://doi.org/10.1029/2021GL094954

Helmus, J. J., & Collis, S. M. (2016). The Python ARM Radar Toolkit (Py-ART), a Library for Working with Weather Radar Data in the Python Programming Language. *Journal of Open Research Software*, *4*(1), 25. https://doi.org/10.5334/jors.119

Holden, Z. A., Swanson, A., Luce, C. H., Jolly, W. M., Maneta, M., Oyler, J. W., et al. (2018). Decreasing fire season precipitation increased recent western US forest wildfire activity. *Proceedings of the National Academy of Sciences*, *115*(36). https://doi.org/10.1073/pnas.1802316115

Homer, C., Dewitz, J., Yang, L., Jin, S., Danielson, P., Xian, G., Coulston, J., et al. (2015). Completion of the 2011 National Land Cover Database for the conterminous United States–representing a decade of land cover change information. *Photogrammetric Engineering & Remote Sensing*, *81*(5), 345-354.

Hong, S. Y., & Lim, J. O. J. (2006). The WRF single-moment 6-class microphysics scheme (WSM6). *Asia-Pacific Journal of Atmospheric Sciences*, 42(2), 129-151.

Iacono, M. J., Delamere, J. S., Mlawer, E. J., Shephard, M. W., Clough, S. A., & Collins, W. D. (2008). Radiative forcing by long-lived greenhouse gases: Calculations with the AER radiative transfer models. *Journal of Geophysical Research*, *113*(D13), D13103. https://doi.org/10.1029/2008JD009944

Juliano, T. W., Lareau, N., Frediani, M. E., Shamsaei, K., Eghdami, M., Kosiba, K., et al. (2023). Toward a Better Understanding of Wildfire Behavior in the Wildland-Urban Interface: A Case Study of the 2021 Marshall Fire. *Geophysical Research Letters, 50*(10), e2022GL101557. https://doi.org/10.1029/2022GL101557

Jiménez, P. A., Dudhia, J., González-Rouco, J. F., Navarro, J., Montávez, J. P., & García-Bustamante, E. (2012). A Revised Scheme for the WRF Surface Layer Formulation. *Monthly Weather Review, 140*(3), 898–918. https://doi.org/10.1175/MWR-D-11-00056.1

Jiménez, P., Muñoz-Esparza, D., & Kosović, B. (2018). A High Resolution Coupled Fire–Atmosphere Forecasting System to Minimize the Impacts of Wildland Fires: Applications to the Chimney Tops II Wildland Event. *Atmosphere*, *9*(5), 197. https://doi.org/10.3390/atmos9050197

Jones, T., Ahmadov, R., James, E., Pereira, G., Freitas, S., & Grell, G. (2022). Prototype of a Warn-on-Forecast System for Smoke (WoFS-Smoke). *Weather and Forecasting*, *37*(7), 1191-1209.

Kochanski, A. K., Jenkins, M. A., Mandel, J., Beezley, J. D., & Krueger, S. K. (2013). Real time simulation of 2007 Santa Ana fires. *Forest Ecology and Management*, *294*, 136–149. https://doi.org/10.1016/j.foreco.2012.12.014

Lareau, N. P., & Clements, C. B. (2016). Environmental controls on pyrocumulus and pyrocumulonimbus initiation and development. *Atmospheric Chemistry and Physics*, *16*(6), 4005–4022. https://doi.org/10.5194/acp-16-4005-2016

Lareau, N. P., & Clements, C. B. (2017). The Mean and Turbulent Properties of a Wildfire Convective Plume. *Journal of Applied Meteorology and Climatology*, *56*(8), 2289–2299. https://doi.org/10.1175/JAMC-D-16-0384.1

Lareau, N. P., Nauslar, N. J., Bentley, E., Roberts, M., Emmerson, S., Brong, B., et al. (2022a). Fire-Generated Tornadic Vortices. *Bulletin of the American Meteorological Society*, *103*(5), E1296–E1320. https://doi.org/10.1175/BAMS-D-21-0199.1

Lareau, N. P., Donohoe, A., Roberts, M., & Ebrahimian, H. (2022b). Tracking Wildfires With Weather Radars. *Journal of Geophysical Research: Atmospheres*, *127*(11). https://doi.org/10.1029/2021JD036158

Lilly, D. (1966a). On the application of the eddy viscosity concept in the Inertial sub-range of turbulence [Application/pdf] (p. 675 KB). UCAR/NCAR. https://doi.org/10.5065/D67H1GGQ

Lilly, D. (1966b). The representation of small-scale turbulence in numerical simulation experiments [Application/pdf] (p. 986 KB). UCAR/NCAR. https://doi.org/10.5065/D62R3PMM

Mandel, J., Beezley, J. D., & Kochanski, A. K. (2011). Coupled atmosphere-wildland fire modeling with WRF 3.3 and SFIRE 2011. *Geoscientific Model Development*, *4*(3), 591–610. https://doi.org/10.5194/gmd-4-591-2011

McCarley, T. R., Hudak, A. T., Sparks, A. M., Vaillant, N. M., Meddens, A. J. H., Trader, L., et al. (2020). Estimating wildfire fuel consumption with multitemporal airborne laser scanning data and demonstrating linkage with MODIS-derived fire radiative energy. *Remote Sensing of Environment*, *251*, 112114. https://doi.org/10.1016/j.rse.2020.112114

Nakanishi, M., & Niino, H. (2006). An Improved Mellor–Yamada Level-3 Model: Its Numerical Stability and Application to a Regional Prediction of Advection Fog. *Boundary-Layer Meteorology*, *119*(2), 397–407. https://doi.org/10.1007/s10546-005-9030-8

Parks, S. A., & Abatzoglou, J. T. (2020). Warmer and Drier Fire Seasons Contribute to Increases in Area Burned at High Severity in Western US Forests From 1985 to 2017. *Geophysical Research Letters*, *47*(22). https://doi.org/10.1029/2020GL089858

Peace, M., Charney, J., & Bally, J. (2020). Lessons Learned from Coupled Fire-Atmosphere Research and Implications for Operational Fire Prediction and Meteorological Products Provided by the Bureau of Meteorology to Australian Fire Agencies. *Atmosphere*, *11*(12), 1380. https://doi.org/10.3390/atmos11121380

Roberts, M., & Lareau, N. (2023). Files for "Sensitivity of Simulated Fire-Generated Circulations to Fuel Load During Large Wildfires". *Harvard Dataverse, V1*. https://doi.org/10.7910/DVN/FEHPIH

Rodriguez, B., Lareau, N. P., Kingsmill, D. E., & Clements, C. B. (2020). Extreme Pyroconvective Updrafts During a Megafire. *Geophysical Research Letters*, *47*(18). https://doi.org/10.1029/2020GL089001

Rollins, M. G. (2009). LANDFIRE: a nationally consistent vegetation, wildland fire, and fuel assessment. *International Journal of Wildland Fire, 18*(3), 235. https://doi.org/10.1071/WF08088

Rothermel, R. C. (1972). A mathematical model for predicting fire spread in wildland fuels. Intermountain Forest & Range Experiment Station, Forest Service.

Scott, J. H., & Burgan, R. E. (2005). *Standard fire behavior fuel models: a comprehensive set for use with Rothermel's surface fire spread model* (No. RMRS-GTR-153) (p. RMRS-GTR-153). Ft. Collins, CO: U.S. Department of Agriculture, Forest Service, Rocky Mountain Research Station. https://doi.org/10.2737/RMRS-GTR-153

Shamsaei, K., Juliano, T. W., Roberts, M., Ebrahimian, H., Kosovic, B., Lareau, N. P., & Taciroglu, E. (2023a). Coupled fire-atmosphere simulation of the 2018 Camp Fire using WRF-Fire. *International Journal of Wildland Fire*, *32*(2), 195–221. https://doi.org/10.1071/WF22013

Shamsaei, K., Juliano, T. W., Roberts, M., Ebrahimian, H., Lareau, N. P., Rowell, E., & Kosovic, B. (2023b). The Role of Fuel Characteristics and Heat Release Formulations in Coupled Fire-Atmosphere Simulation. *Fire, 6*(7), 264. https://doi.org/10.3390/fire6070264

Schmidt, C. C., Hoffman, J., Prins, E., Lindstrom, S. (2012). GOES-R Advanced Baseline Imager (ABI) Algorithm Theoretical Basis Document For Fire / Hot Spot Characterization. NOAA NESDIS Center for Satellite Applications and Research.

Skamarock, W. C., Klemp, J. B. (2008). A time-split nonhydrostatic atmospheric model for weather research and forecasting applications. *Journal of Computational Physics, 227*(7), 3465-3485. https://doi.org/10.1016/j.jcp.2007.01.037

Skamarock, W. C., Klemp, J. B., Dudhia, J., Gill, D. O., Liu, Z., Berner, J., et al. (2019). A Description of the advanced research WRF version 4 (Technical Report). NCAR Tech. Note NCAR/TN-556+STR.

Stephens, S. L., Bernal, A. A., Collins, B. M., Finney, M. A., Lautenberger, C., & Saah, D. (2022). Mass fire behavior created by extensive tree mortality and high tree density not predicted by operational fire behavior models in the southern Sierra Nevada. *Forest Ecology and Management*, *518*, 120258. https://doi.org/10.1016/j.foreco.2022.120258

USDA Forest Service. (2021). *Caldor Fire Burned Area Emergency Response (BAER) Assessment Report*. Retrieved from https://www.fs.usda.gov/Internet/FSE_DOCUMENTS/fseprd963659.pdf

Val Martin, M., Kahn, R. A., Logan, J. A., Paugam, R., Wooster, M., and Ichoku, C. (2012), Space-based observational constraints for 1-D fire smoke plume-rise models, *J. Geophys. Res.*, 117, D22204, doi:10.1029/2012JD018370.

Van Zyl, J. J. (2001). The Shuttle Radar Topography Mission (SRTM): a breakthrough in remote sensing of topography. *Acta Astronautica*, *48*(5–12), 559–565. https://doi.org/10.1016/S0094-5765(01)00020-0

Westerling, A. L., Hidalgo, H. G., Cayan, D. R., & Swetnam, T. W. (2006). Warming and Earlier Spring Increase Western U.S. Forest Wildfire Activity. *Science*, *313*(5789), 940–943. https://doi.org/10.1126/science.1128834

Westerling, A. L. (2016). Increasing western US forest wildfire activity: sensitivity to changes in the timing of spring. *Philosophical Transactions of the Royal Society B: Biological Sciences*, *371*(1696), 20150178. https://doi.org/10.1098/rstb.2015.0178

Williams, J. (2013). Exploring the onset of high-impact mega-fires through a forest land management prism. *Forest Ecology and Management*, *294*, 4–10. https://doi.org/10.1016/j.foreco.2012.06.030